ACS NANO
Cite This: ACS Nano 2019, 13, 6308–6318
www.acsnano.org

ARTICLE

Single Molecule Identification and Quantification of Glycosaminoglycans Using Solid-State Nanopores

JongOne Im,[†,§] Stuart Lindsay,[*,†,‡,§] Xu Wang,[*,‡] and Peiming Zhang[*,†]

[†]Biodesign Institute, [‡]School of Molecular Sciences, and [§]Department of Physics, Arizona State University, Tempe, Arizona 85287, United States

Supporting Information

ABSTRACT: Glycosaminoglycans (GAGs) are a class of polysaccharides with potent biological activities. Due to their complex and heterogeneous composition, varied charge, polydispersity, and presence of isobaric stereoisomers, the analysis of GAG samples poses considerable challenges to current analytical techniques. In the present study, we combined solid-state nanopores—a single molecule sensor with a support vector machine (SVM)—a machine learning algorithm for the analysis of GAGs. Our results indicate that the nanopore/SVM technique could distinguish between monodisperse fragments of heparin and chondroitin sulfate with high accuracy (>90%), allowing as low as 0.8% (w/w) of chondroitin sulfate impurities in a heparin sample to be detected. In addition, the nanopore/SVM technique distinguished between unfractionated heparin (UFH) and enoxaparin (low molecular weight heparin) with an accuracy of ∼94% on average. With a reference sample for calibration, a nanopore could achieve nanomolar sensitivity and a 5-Log dynamic range. We were able to quantify heparin with reasonable accuracy using multiple nanopores. Our studies demonstrate the potential of the nanopore/SVM technique to quantify and identify GAGs.

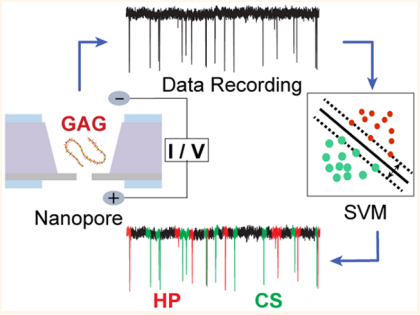

KEYWORDS: *nanopore, glycosaminoglycan, heparin, machine learning, SVM*

Glycosaminoglycans (GAGs) are a class of linear polysaccharides ubiquitous to all mammals. Although GAGs can be found in most cellular compartments, they mostly occur on cell surfaces and in the extracellular matrix. Biologically, GAGs play regulatory roles in physiological and pathological processes such as cell growth and development,[1] cancer progression,[2−4] neurodegenerative diseases,[5−7] wound healing,[8] and angiogenesis.[9] Moreover, the sulfated GAGs may represent a type of promising biomaterials for tissue engineering, repair, and reconstruction.[10] Structurally, a naturally occurring GAG is a polydisperse linear polymer characterized by disaccharide repeats. The composition of the disaccharide is used to classify GAGs. For example, heparin is mostly composed of α-L-iduronate-(1 → 4)-α-D-glucosamine disaccharides, whereas chondroitin sulfate (CS) is mostly composed of β-L-glucuronate-(1 → 3)-β-D-galatosamine disaccharides. Nonetheless, the structure of GAGs is complicated as a result of variations in the length of the chains, semirandom epimerization, and sulfation of the sugars due to a template independent enzymatic process *in vivo*. These structural complexities pose significant challenges for the compositional analysis of GAGs.[11−14] NMR remains one of the most effective techniques to unambiguously identify glycosidic linkages and positions of the sulfates in GAGs. It is a de facto method for detecting traces of oversulfated chondroitin sulfate (OSCS) in heparin, approved by the US pharmacopoeia for analysis of low molecular weight and highly homogeneous heparins. Mass spectrometry (MS) based hyphenated methods like liquid chromatography (LC)-MS[15,16] and capillary electrophoresis (CE)-MS[17−19] are also commonly used techniques for the separation and identification of GAGs. However, the mass analysis is inefficient for distinguishing between isobaric isomers which commonly exist in GAGs. Either LC or CE alone is also inadequate because of their limited resolvability of a mixture of charged isomers.

Nanopores, made of either biological or inorganic materials with orifices of nanometer diameters and depth,[20] have been exploited as a single molecule sensor for analysis of DNA,[21] RNA,[22−24] proteins,[25,26] and unsulfated GAG polysaccharides, such as hyaluronan.[27,28] Recently, Dwyer and co-workers reported on the analysis of two sulfated GAGs—heparin and OSCS using silicon nitride nanopore.[29] They demonstrate that heparin and OSCS mixed in equal proportions can be qualitatively identified either by current blockade magnitudes

Received: January 23, 2019
Accepted: May 23, 2019
Published: May 23, 2019

DOI: 10.1021/acsnano.9b00618
ACS Nano 2019, 13, 6308–6318

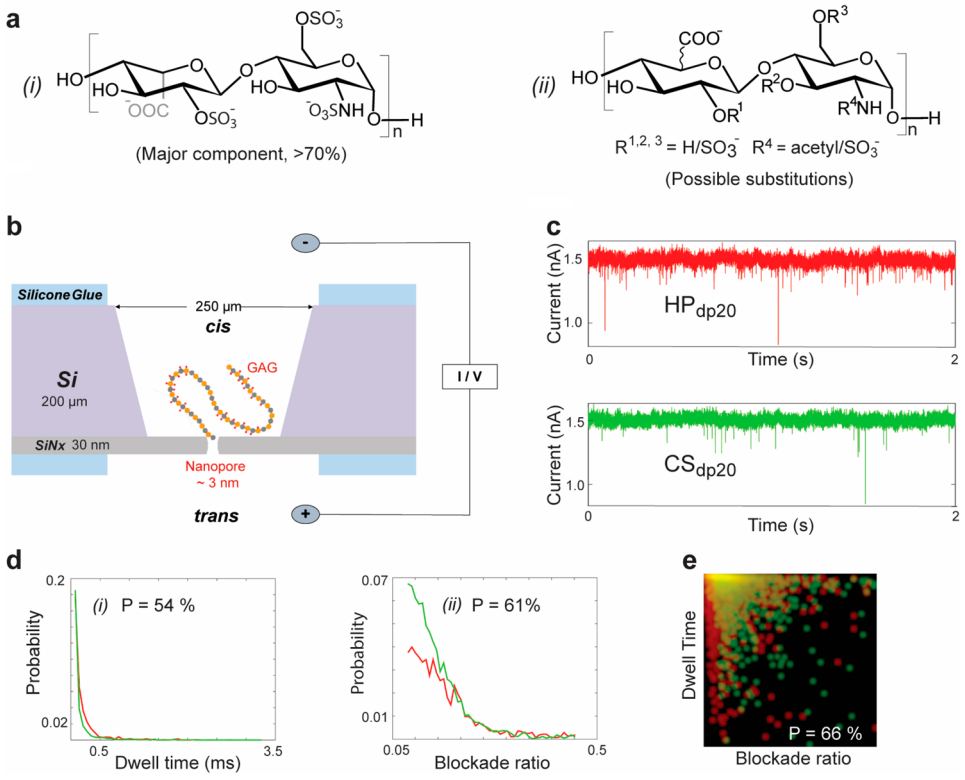

Figure 1. (a) Structural characteristics of heparin. (*i*) the major disaccharide; (*ii*) possible substitution patterns. (b) Schematic illustration of a solid-state nanopore device for translocation of linear negatively charged polysaccharides (the *cis*-side electrode is grounded). (c) Ionic current traces of HP_{dp20} and CS_{dp20} translocating through a nanopore. (d) Distributions of dwell times and blockade ratios for HP_{dp20} and CS_{dp20}; *P* is the probability of separating the two sets of data. (e) A two-dimensional plot of both dwell time and blockade for HPdp20 and CS_{dp20}. (Red denotes HP_{dp20} and green CS_{dp20}).

or blockade durations despite considerable overlaps of these parameter distributions in a 2D scatter plot.

We have been working on employing a solid-state nanopore as a molecular transporter for our nanoelectronic technology to sequence GAGs.[30] We chose the highly sulfated GAG molecule heparin as our first target, which is a potent anticoagulant[31] and one of the most commonly used blood thinners in medicine. The low molecular weight heparins (LMWHs) are a major type of heparin for antithrombotic use[32] and the first line choice for cancer-associated thrombosis.[33,34] Heparin also has the most complex structure among GAGs. Although the disaccharide 2-*O*-sulfo-α-L-iduronate-(1 → 4)-α-D-glucosamine-*N*,6-*O*-disulfate-(1 → 4) accounts for 70−90% of disaccharide units in heparin (Figure 1a, *i*),[35] it may contain 32 possible disaccharides (Figure 1a, *ii*),[36] so a dodecasaccharide fragment of heparin could have more than 1 million different sequences. This degree of complexity renders the accurate analysis of heparin and other GAGs beyond the reach of current analytical technologies. The detection of the GAG contamination or impurities in medicinal heparin remains a significant challenge. As a consequence, the 2007−2008 crisis of heparin contaminated by OSCS resulted in the death of more than 80 people in the United States alone.[37] Therefore, a rapid and cost-effective method for identifying heparin and analogous GAGs is sorely needed for routine quality control.

In the present study, we demonstrate that the solid-state nanopore can effectively translocate GAGs and the nanopore data can be used to identify GAGs with the aid of machine learning. As illustrated in Figure 1b, when a negatively charged GAG molecule translocates through a silicon nitride nanopore under a voltage bias, it causes a transient blockade of the ionic current, evoking a current spike—an event that carries information on the structure or physical properties of an individual GAG molecule. Figure 1c shows current traces of monodispersed heparin (HP_{dp20}) and CS (CS_{dp20}) fragments generated by nanopore measurements. Herein, HP_{dp20} denotes a heparin fragment that is composed of 20 sugar units (dp: degree of polymerization) and CS_{dp20} denotes a chondroitin sulfate fragment comprised of 10 disaccharide units of β-D-glucuronic acid-(1 → 3)-β-*N*-acetylgalactosamine-4-sulfate-(1 → 4).[38] To have insight into the nanopore data, we first characterized each individual signal by its blockade ratio (or a ratio of spike amplitude to baseline ionic current) and dwell time (width of the spike). Each of these individual parameters exhibited similar distributions between HP_{dp20} and CS_{dp20}. As shown in Figure 1d, the probability of separating HP_{dp20} from CS_{dp20} by their dwell times is about 54% (similar to a random pick that is 50%) and the probability by their blockade ratios is about 61% (slightly better than a random pick). When these two parameters are plotted together as the probability density for the simultaneous appearance of a pair of values in a given spike, the likelihood of correctly classifying each event improves to >66% (Figure 1e). Thus, one may envisage achieving higher accuracy if a high dimensional parameter space is used to classify the nanopore data. Winters-Hilt and Akeson pioneered the use of machine learning for analysis of the nanopore data, engaging support vector machines (SVMs) as a DNA base discriminator.[39] SVM is a supervised learning model to separate different classes in a hyperdimensional space

DOI: 10.1021/acsnano.9b00618
ACS Nano 2019, 13, 6308−6318

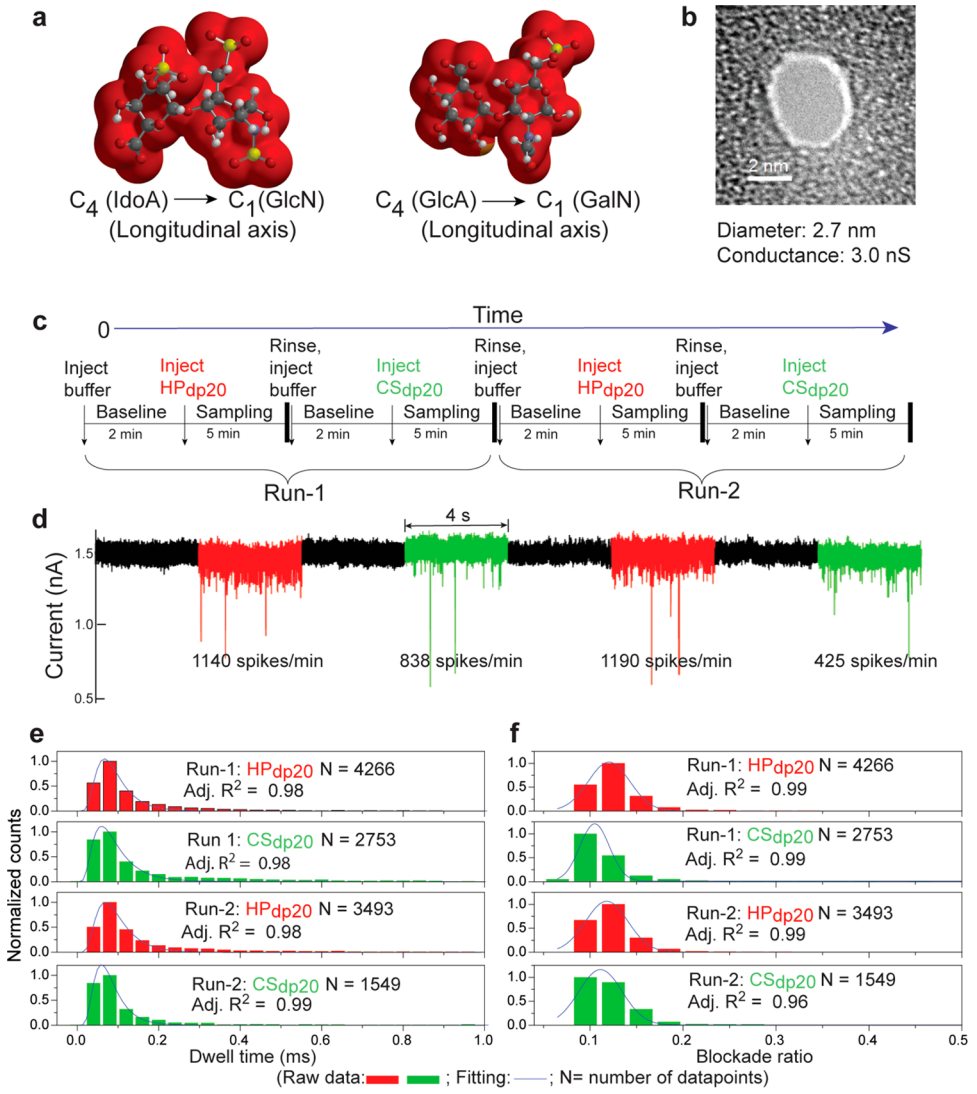

Figure 2. (a) DFT (density functional theory) structures and electrostatic potential maps of HP_{dp20} and CS_{dp20} disaccharides, in which the potential is scaled in an order of red (the most negative) < orange < yellow < green < blue (the most positive). (b) A TEM image of the solid-state nanopore in the silicon nitride membrane. (c) A workflow for a multiple run experiment, which was carried out in a 0.4 M KCl phosphate buffer, pH 7.4, with a concentration of 100 nM for both samples. (d) Typical ionic current traces for the buffer, HP_{dp20} in the buffer, and CS_{dp20} in the buffer, recorded with a voltage bias of 500 mV. (e) Histograms of dwell times with their log normal fitting curves for HP_{dp20} and CS_{dp20} for different runs. (f) Histograms of blockade ratios with their Gaussian fitting curves for HP_{dp20} and CS_{dp20} for different runs.

and has become a tool for analyzing data from single molecule techniques. Previously, we successfully exploited SVM to identify mono- and disaccharides by classifying their electron tunneling data.[30] In the present work, we extended it to the analysis of solid-state nanopore data from translocation of GAG polysaccharides.

RESULTS AND DISCUSSION

Nanopore/SVM Identification of HP_{dp20} and CS_{dp20}. As mentioned above, we first analyzed two monodisperse GAG samples—HP_{dp20} and CS_{dp20}—using a solid-state nanopore. Beforehand, all of the GAG samples we acquired were characterized by size exclusion and strong anion-exchange (SAX) HPLC (Figure S1, Supporting Information). Despite similar molecular weights between each other, HP_{dp20} is more negatively charged than CS_{dp20}. Density functional theory (DFT) calculation shows that the most common disaccharide units in heparin and CS have distinct structural features, albeit both are highly negatively charged (displayed in red, Figure 2a). This modeling study suggests these two GAGs should be distinguishable by a nanopore. The solid-state nanopores we used were fabricated in a silicon nitride membrane by drilling with a transmission electron microscope (TEM). It has been reported that such nanopores most likely have an hourglass-shaped geometry.[40] By $I-V$ scans, we observed rectified currents at pH 8, not at pH 7.5 and 6.5 (Figure S2, Supporting Information). The silicon nitride surface is zwitterionic, and its isoelectric point (pI) intrinsically relies on the ratio of Si−OH to both $Si-NH_2$ and Si_2NH on the surface, varying from pH 3.0 to 9.0.[41] Thus, our nanopores probably had their pIs between pH 7.5 and 6.5, where its surface had no net electrical charge. The current rectification at pH 8 may be explained by a negative charge dominated surface with an asymmetric nanopore geometry.[42] We carried out our translocation experiments in a phosphate buffer, pH ∼ 7.4. Besides, we

DOI: 10.1021/acsnano.9b00618
ACS Nano 2019, 13, 6308−6318

Table 1. Statistical Parameters Derived from Curve Fitting of Raw Data in Figure 2e and f[a]

	HP_{dp20}				CS_{dp20}			
	dwell time (ms)		blockade ratio		dwell time (ms)		blockade ratio	
	median	mean	mean	σ	median	mean	mean	σ
run 1	0.083	0.092	0.120	0.027	0.080	0.092	0.105	0.019
run 2	0.087	0.098	0.118	0.027	0.073	0.081	0.111	0.028

[a]Note: (1) all adj. R^2 > 95%; (2) all fitting errors for median < ±1.0% and for mean < ±1.0%; (3) all fitting errors for peak < ±0.1% and for width < ±0.2%.

Table 2. Accuracy of SVM Calling Individual Spikes

	SVM training				SVM calling (%)				
					remaining 50% data		untrained data		
	training data set	analyte	number of features	training accuracy	HP_{dp20}	CS_{dp20}		HP_{dp20}	CS_{dp20}
SVM-2	50% of run 1	HP_{dp20}	11	100	**93.2**	7.9	run 2	**94.2**	4.9
		CS_{dp20}			6.8	**92.1**		5.8	**95.1**
SVM-4	50% of run 2	HP_{dp20}	11	100	**96.2**	6.0	run 1	**93.7**	8.8
		CS_{dp20}			3.8	**94.0**		6.3	**91.2**

chose 30 nm thick nanopores for this study because it provided some measurement advantages over those with a thickness of 15 and 50 nm (section 1 and Figure S3-1, Supporting Information). By a reverse bias experiment, we confirmed that HP_{dp20} translocated through a solid-state nanopore of ∼3.0 nm in diameter (section 2 and Figure S3-2, Supporting Information). Following these benchmark works, we conducted a serial measurement on HP_{dp20} and CS_{dp20} with a freshly fabricated silicon nitride nanopore (see Figure 2b for its TEM image). As illustrated in Figure 2c, the two GAG samples were measured in run 1 and then repeated in run 2, where a process of rinsing nanopore and stabilizing (or recovering) baseline was involved before each measurement. Figure 2d displays typical traces of ionic currents recorded from the nanopore measurement (black, a 0.4 M KCl phosphate buffer; red, 100 nM HP_{dp20} in the buffer; green, 100 nM CS_{dp20} in the buffer), where each spike may represent a single molecule translocating or bumping event. First, we examined the translocation efficiency defined by an event rate (events/min) and found that the event rates for HP_{dp20} are always higher than those for CS_{dp20}. It may be explained by the fact that the former is more negatively charged than the latter. However, the event rate fluctuated from run to run significantly for both HP_{dp20} and CS_{dp20}. We found that HP_{dp20} always had a higher event rate in run 2 than in run 1, whereas CS_{dp20} had a lower event rate in run 2 than in run 1 (Table S1).

We analyzed the nanopore data mentioned in Figure 2d by determining dwell times and blockade ratios of individual spikes (see the note in the Supporting Information file for instructions on obtaining source data files), plotting them in histograms (Figure 2e and f), in which each data set is composed of more than a thousand data points. The distributions of dwell times were best fit to the log normal function, whereas those for blockade ratios were best fit to the Gaussian function, from which statistical values of these parameters were derived for both HP_{dp20} and CS_{dp20} and summarized in Table 1. These parameters are only marginally different from run 1 to run 2 for both HP_{dp20} and CS_{dp20}. In this respect, the nanopore measurement is reasonably reproducible. Statistically, each parameter distribution shows a significant overlap between HP_{dp20} and CS_{dp20} (see Figure 2e and f). As mentioned above, these primary parameters are not sufficient for discriminating among monodisperse GAG samples unambiguously.

Therefore, we specifically engaged SVM for the identification of GAGs with nanopore data. SVM is a method that utilizes many independent parameters (or features) to classify data in a hyperdimensional space. For the machine-learning-based analysis, we first extracted a series of features by means of Fourier transform (FFT) and cepstrum transform of the nanopore data that were recorded in the time domain (see the Methods section and Table S2 and Figure S4, Supporting Information) to index each individual spike. With these features, we randomly took 50% of the nanopore data either from run 1 or run 2 to train SVM until it could successfully assign each of the spikes in the training data to its corresponding GAG analyte with 100% accuracy (Table 2). We found that the SVM could be trained with different combinations of features to achieve the 100% accuracy; that is, many of the different SVMs can be created using the same data set (Tables S3-1 and S3-2, Supporting Information). To score these trained SVMs, we engaged them to call the remaining 50% of the nanopore data by scaling a perfect calling accuracy to 100%. As shown in Table 2, **SVM-2** has the highest rating of 92.7% among those trained with the run 1 data and **SVM-4** has the highest score of 95.1% among those trained with the run 2 data on average. Then, we used **SVM-2** to call the run 2 data, which identified HP_{dp20} and CS_{dp20} with an accuracy of 94.2% and 95.1%, respectively. In turn, **SVM-4** called HP_{dp20} and CS_{dp20} in the run 1 data with an accuracy of 93.7% and 91.2%, respectively. As a result, SVM called these two GAGs with high accuracy. We should point out that (1) the accuracy is related to SVM calling each single spike. Assuming the errors occur randomly, one may expect that it can be further improved by multiple nanopore measurements; (2) the nanopore data may be a sum of molecular bumping and translocating events. The above results suggest that both bumping and translocating data can be used by the SVM to identify the GAG molecules; (3) the fine features in translocation signals may reflect the translational movements of the molecule in a pore and are highly dependent on the geometry of the pore. As a result, SVM created using one set of training data may only be

DOI: 10.1021/acsnano.9b00618
ACS Nano 2019, 13, 6308−6318

Table 3. CS_{dp20} Molar Percentages in Mixtures Determined by the Nanopore/SVM Method

		molar percentage of CS_{dp20} in HP_{dp20}				
		1%	5%	10%	20%	50%
nanopore	SVM score	percentage (%) of CS_{dp20} determined by SVM calling				
pore 1	98.3					46.1
pore 1[a]	100					57.2
pore 2	93.3	1.4		11.1		
pore 3	94.0	3.0	7.4			
pore 4	84.1				23.2	
pore 5	83.3	0.5	3.9			
pore 6	80.8			9.3	21.9	
average ± SEM[b]		1.6 ± 0.7	5.7 ± 1.8	10.2 ± 0.9	22.6 ± 0.7	51.7 ± 5.6
CV[c] (%)		77.5	43.8	12.5	4.1	15.2
error rate[d] (%)		60.0	14.0	2.0	13.0	3.4

[a]A repeat of the measurement in pore 1. [b]SEM: standard error of mean. [c]CV: coefficient of variation. [d]Error rate = ⟨averaged called percentage − molar percentage in sample⟩/molar percentage in sample.

applicable to the data collected with nanopores of similar physical characteristics.

Detection of CS_{dp20} in a Binary Mixture. We further tested the nanopore/SVM method for its potential use in the detection of impurities in a heparin product. To prove the principle, we mixed CS_{dp20} with HP_{dp20} in a molar percentage of 1, 5, 10, 20, and 50%, respectively. The nanopore measurement was carried out in the same way as described above, following a sequence of CS_{dp20}, HP_{dp20}, and the mixture. Here, the pure CS_{dp20} and HP_{dp20} samples were used as standards to produce the reference data for training SVM. Under our experimental conditions, the nanopore was easily blocked by these GAG samples. However, we managed to finish the measurement using multiple nanopores. As shown in Table 3, six nanopores were used in this study, and each mixture was measured at least twice either by the same nanopore or different nanopores. Following the nanopore measurement, we trained SVM with data from the reference samples in the same manner as described above and engaged the SVMs to call HP_{dp20} and CS_{dp20} in the mixtures from their nanopore data (Table S4, Supporting Information). Table 3 lists the percentages of CS_{dp20} in the different mixtures determined by the best-scored SVM. First, we observed that, although the measured percentage of CS_{dp20} varies more or less from nanopore to nanopore, which may be attributed to the variations in the geometry of these nanopores (Figure S5, Supporting Information), its average is close to the one actually existing in the mixture. A plot of the average called percentages against the molar percent of CS_{dp20} in the mixtures fits a linear function (Figure 3). With its intercept fixed at the origin, the fit gives the trend line with a slope of ~1.1, slightly higher than 1.0—the best-case scenario, which may result in an overestimate of CS_{dp20} by 10%. Overall, the variations among different pores decrease with increases of CS_{dp20} percentage in the mixture, as do the SVM calling error rates (based on CV values and error rates in Table 3). This study demonstrates that, with our current setup, the nanopore/SVM method can identify CS_{dp20} in a mixture down to ~1% in molar percentage, equal to a weight percentage of 0.8% (w/w). This sensitivity is comparable to 500 MHz NMR, which has a limit of detection of 0.1% (w/w) for oversulfated chondroitin sulfate (OSCS).[43] However, NMR requires milligrams of sample/0.7 mL of solvent for the measurement so that the OSCS ought to be at least at a microgram level in the sample. For the nanopore

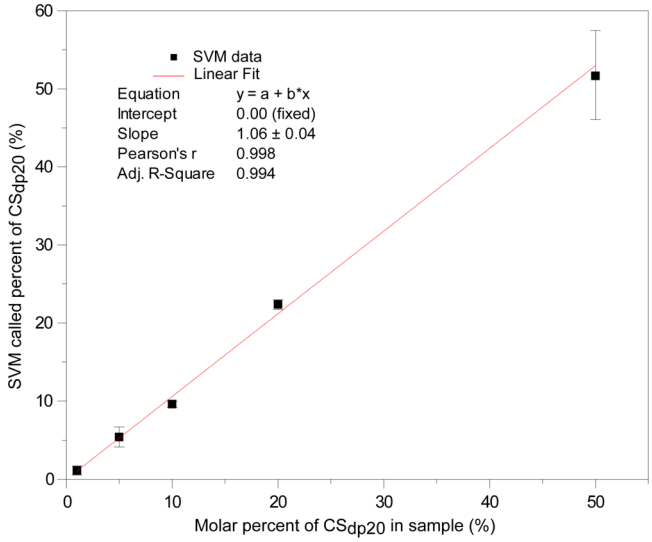

Figure 3. Percentages of CSdp20 determined by the nanopore/SVM method against its compositions in the mixture samples.

measurement, we only used 0.1 mL of solution with the mixture containing a total GAG concentration of 100 nM. To measure a 1% mixture, we only needed 0.4 ng of CS_{dp20} for the nanopore detection.

Identification of Unfractionated Heparin and Enoxaparin. To explore its potential applications in pharmaceutical production, we tested the nanopore/SVM method on two of the clinically used GAG samples—unfractionated heparin (UFH) and the LWMH enoxaparin.[44] In contrast to HP_{dp20} and CS_{dp20}, both UFH and enoxaparin are polydisperse. Enoxaparin has a smaller molecular weight than UFH, containing an unsaturated uronate residue at its nonreducing end as well as an amino sugar or a 1,6-anhydro amino sugar at its reducing end (Figure 4a). We sequentially measured HP_{dp20}, CS_{dp20}, enoxaparin, and UFH at a 1.0 μM concentration using a freshly drilled nanopore of ~3 nm in diameter (Figure 4b). Between the measurements, there was a process of rinsing and baseline recovery. Figure 4c displays the typical current traces of these GAG products recorded by the nanopore and their event rates which follow an order of UFH > HP_{dp20} > enoxaparin > CS_{dp20}. First, we characterized the current spikes of each product by their dwell times and blockade ratios, which were then placed in a 2D scatter plot

DOI: 10.1021/acsnano.9b00618
ACS Nano 2019, 13, 6308−6318

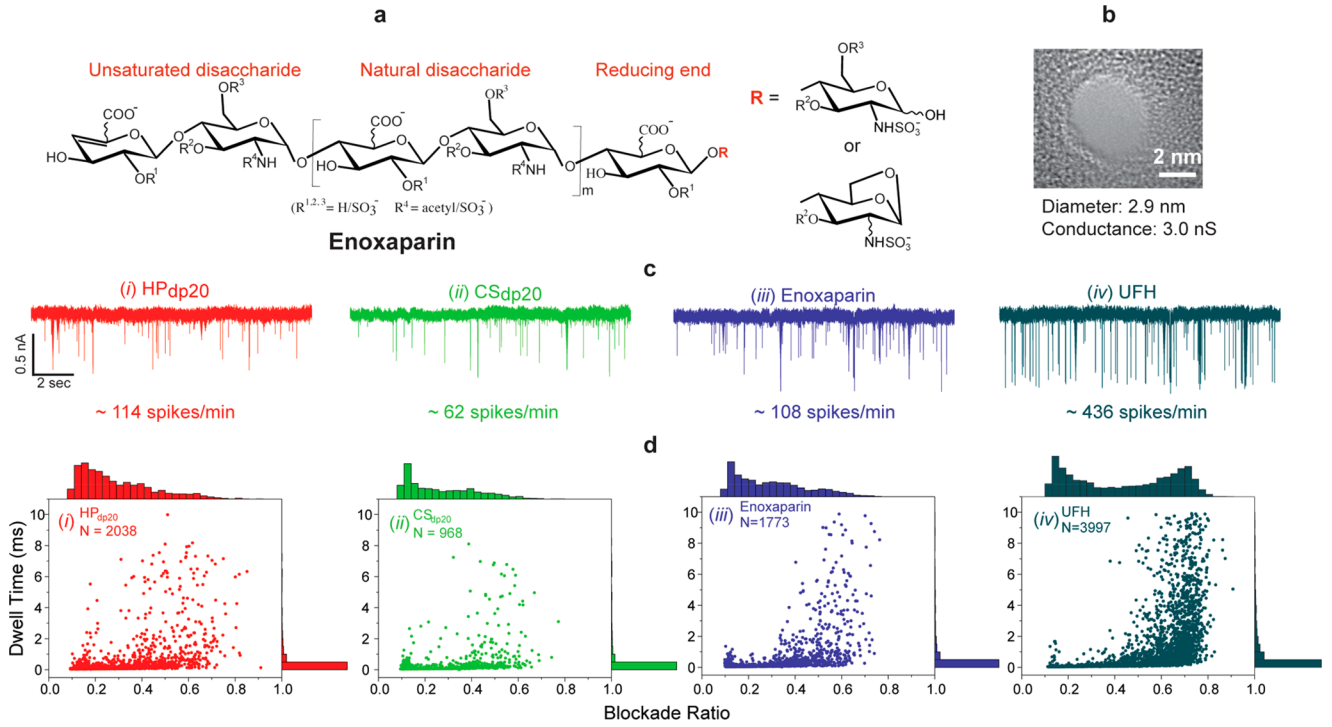

Figure 4. (a) Chemical structure of enoxaparin. (b) TEM image of the nanopore used in the measurement. (c) Typical ionic current traces of HP_{dp20}, CS_{dp20}, enoxaparin, and UFH recorded under a voltage bias of 500 mV in the 0.4 M KCl phosphate buffer, pH 7.4. (d) Scatter plots of dwell time vs current blockade ratio, accompanied by their respective marginal histograms.

Table 4. Accuracy of SVM Calling Heparins and CS_{dp20}

			identification accuracy[a] (%)				
entry	entity	training accuracy (%)	UFH	CS_{dp20}	Enox	HP_{dp20}	average
1	UFH vs CS_{dp20}	100	94.6 ± 1.2	91.0 ± 1.5			92.5 ± 1.0
2	UFH vs Enox	100	95.9 ± 0.9		92.9 ± 0.9		94.4 ± 0.6
3	UFH vs HP_{dp20}	100	87.2 ± 1.6			82.1 ± 1.4	84.7 ± 1.1
4	Enox vs CS_{dp20}	100		73.8 ± 2.7	72.1 ± 1.7		73.0 ± 1.6
5	Enox vs HP_{dp20}	100			88.4 ± 2.3	86.4 ± 1.3	87.4 ± 1.3
6	HP_{dp20} vs CS_{dp20}	100		88.7 ± 1.8		83.3 ± 1.4	86.0 ± 1.1
7	pool of four	100	80.6 ± 1.6	65.1 ± 2.6	65.2 ± 3.3	64.8 ± 3.3	68.9 ± 1.4

[a]Each value is an average of three calls by the SVMs trained from three randomly selected subsets of data.

(Figure 4d). Interestingly, unlike other GAG samples, UFH displays a two-peaked distribution in its blockade ratios, one of which is located at the low end between 0.1 and 0.2, similar to those for the other GAGs, and the other located between 0.6 and 0.8, which can be attributed to a significant portion of high molecular weight polymer in UFH. Also, these GAG products have their dwell times in a range of 60−90 μs (Table S5, Supporting Information) on average. Since the data was recorded at a sampling rate of 500 kHz with 100 kHz low pass frequency bandwidth, the differences among those dwell times may not be significant.

To identify these GAGs, we randomly selected 50% of the data from each data set to train the SVM with up to 88 available signal features and then applied the trained SVM to classify the remaining 50% data. This allowed us to quickly determine how effective SVM is in identifying GAGs without going through laborious multiple runs for the proof of concept study. At first, we attempted to distinguish between the four products in pairs by SVM. All SVMs were trained to be capable of identifying individual spikes in the training data with 100% accuracy. As shown in Table 4, both UFH and CS_{dp20} were called with an accuracy of 94.6% and 91.0%, respectively, 92.5% on average (entry 1); UFH and enoxaparin (designated as Enox) were called with an accuracy of ~96% and 93%, respectively (entry 2). However, UFH and HP_{dp20} were distinguished with a lower accuracy of ~85% on average (entry 3). For calling Enox, the SVM distinguished between Enox and HP_{dp20} (entry 5) marginally better than between UFH and HP_{dp20}.

However, it distinguished between Enox and CS_{dp20} with only an averaged accuracy of ~73% (entry 4), significantly lower than it did between UFH and CS_{dp20}. This may be explained by the scatter plots in Figure 4d, where data points of CS_{dp20} overlap with those of enoxaparin more than those of UFH. Interestingly, SVM distinguished between HP_{dp20} and CS_{dp20} (entry 6) better than between Enox and CS_{dp20} (entry 4), even though HP_{dp20} has a molecular weight distribution overlapped with CS_{dp20}'s more than enoxaparin does with CS_{dp20}'s (Figure S1A, Supporting Information). Thus, the result may be better explained on the basis of their SAX-HPLC chromatograms (Figure S1-B, Supporting Information), where HP_{dp20} has its charged fragments overlapped with CS_{dp20}'s less

DOI: 10.1021/acsnano.9b00618
ACS Nano 2019, 13, 6308−6318

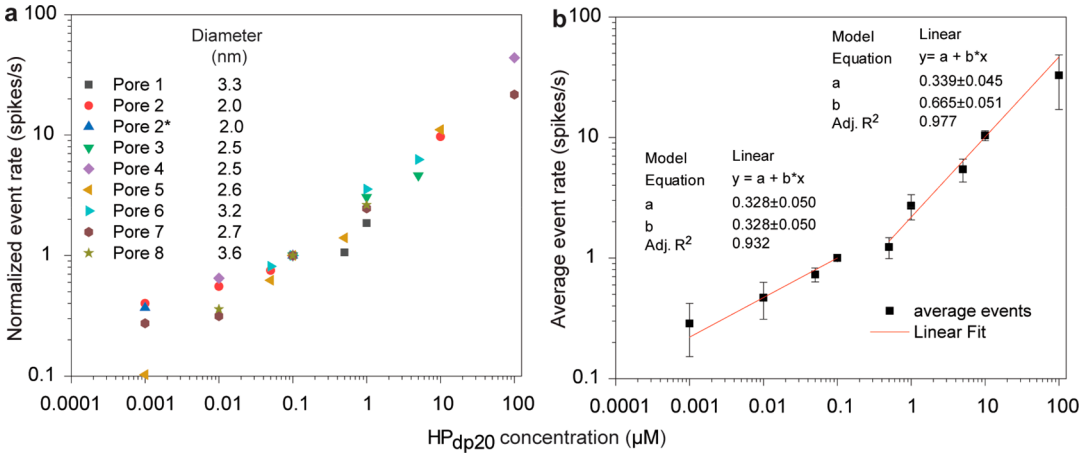

Figure 5. (a) Plot of event rates vs the concentrations of HP_{dp20} from individual nanopores. (b) Plot of averaged event rates vs the concentrations of HP_{dp20} with their fitting lines. For the linear function, y = log(event rate) and x = log(conc).

Table 5. Testing the Fitting Functions for Determination of HP_{dp20} Concentration by Nanopores

Pore	TEM image	Concentration Measurement				
		Sample conc. (μM)	0.01	0.05	1.0	5.0
9	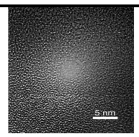	Event rate* (spikes/s)	0.430	0.637	1.523	6.175
		Derived conc. (μM)	0.008	0.025	0.6	4.8
10	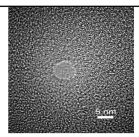	Event rate* (spikes/s)	0.509	-	2.466	-
		Derived conc. (μM)	0.013	-	1.20	-
		Average (μM)	0.011±0.004		0.90±0.42	

*Normalized event rates and see Table S8 in the Supporting Information for their raw data.

than Enox does. We also noticed that the nanopore shown in Figure 2b had a higher accuracy for distinguishing between HP_{dp20} and CS_{dp20} than the one in Figure 4b. From their TEM images, these two nanopores had different shapes and diameters, which may contribute to the difference in accuracy. Furthermore, we also tested SVM for calling all four GAG products from a pool of nanopore data. The SVM called UFH with an accuracy of ~80% and the rest with an accuracy of around ~65% (entry 7). These calling accuracies are statistically significant because the probability of a random pick would only be 25%. The better calling accuracy for UHF could be explained by the fact that UHF contains a portion of blockade currents well separated from those of the rest of the GAGs, which are overlapped with one another (Figure 4d). Nonetheless, the low calling accuracy indicates that the data from a single nanopore would not be sufficient for SVM to call multiple GAGs all at once. To address the issue, we will explore a nanopore array approach to increase the output of data and try different machine learning algorithms, such as deep learning.[45]

Quantification of HP_{dp20}. Lastly, we explored the use of a solid-state nanopore for the quantitation of sulfated GAGs. Dwyer et al. have demonstrated that the event rates in a nanopore linearly increased with concentrations of heparin in a range from 0.25 to 1.25 μM (a 5-fold change).[29] In our study, we first created a calibration curve (Figure 5b) using multiple nanopores to measure a series of HP_{dp20} solutions with their concentrations in a range of 100 μM to 1.0 nM prepared by diluting a stock solution. The measurement on each concentration was repeated at least once in the same or a different nanopore. From each of the nanopore data sets, an event rate (spikes/s) was determined by dividing the ionic current signals above a threshold by time (Table S6, Supporting Information). Our first observation is the event rate of a sample varied from nanopore to nanopore. That may be attributed to different diameters and shapes among these nanopores even though they were fabricated under the same TEM conditions (Figure S6). To compare the event rates between different nanopores, we normalized all of the event rates measured with the same nanopore by referencing the one at 0.1 μM as 1.0 (Table S7, Supporting Information). The normalized data were plotted on a log–log scale (Figure 5a), an approach that has been used to analyze the data of DNA translocation through nanopores.[46,47] In turn, the averaged event rate for each of the concentrations from different nanopores was plotted, shown in Figure 5b. The averages were fitted to two different linear functions separately, which is statistically more satisfactory than an exponential or Langmuir fitting. The results indicate that the event rate changes more rapidly in the μM region than in the nM region. On the basis

DOI: 10.1021/acsnano.9b00618
ACS Nano 2019, 13, 6308–6318

of such a linear standard curve, we estimate that the nanopore measurement has a sensitivity down to a nM level with a 5-Log dynamic range for the detection of HP_{dp20} under our current setup.

To test the accuracy of the method, we determined the concentrations of HP_{dp20} samples using two freshly fabricated nanopores. In the same way as mentioned above, 0.1 μM HP_{dp20} sample was used as a standard and its event rates in the nanopores were referenced as 1.0 (Table S8, Supporting Information). As shown in Table 5, we first measured four HP_{dp20} samples for their event rates with a nanopore (designated as pore 9), from which their concentrations were derived by applying one of the two functions in Figure 5b, and then repeated the measurement with two of the samples using the second nanopore (designated as pore 10). The results show that the concentration determined by different nanopores varied, deviating considerably from the actual value of the tested sample. For example, the 0.01 μM sample was determined as 0.008 μM by pore 9 and 0.013 μM by pore 10. However, the average of these two measurements is 0.011, only 10% off from the actual concentration. For the 1.0 μM sample, the average of measurements by these two nanopores is 0.9 μM, just 10% lower than expected. At the higher concentration, 5.0 μM in this study, the concentration determined by a single nanopore measurement only deviated from the actual one by 6%. These results show that the nanopore can potentially be used to quantify sulfated GAG samples by introducing a reference sample for the nanopore calibration. Besides, repeatednanopore measurements are needed to achieving high accuracy, especially when the sample concentration is below the μM range.

CONCLUSIONS

In the present study, we combined the nanopore measurement with machine learning (SVM) for identification of heparin and CS. Our data show that the nanopore/SVM method can effectively distinguish between different heparin preparations as well as between monodisperse heparin and CS. We were able to identify CS_{dp20} in its mixtures with HP_{dp20} at a level down to 0.8% (w/w) using the nanopore/SVM method, comparable to the NMR technique for detection of OSCS. In contrast to NMR, which requires bulky and expensive instruments as well as more material, the nanopore measurement provides a cost-effective method and potentially a hand-held electronic device for the detection and analysis of these GAG molecules. Although we only examined monodisperse heparin and CS in this study, the results indicate translocation signals contain information on the sulfate content as well as the size of the molecule. Given the fact that heparin and CS have drastic differences in both size and sulfation density, we are hopeful that the technique can be used to distinguish between heterogeneous samples given proper calibration standards. Indeed, the demonstration that UFH can be easily distinguished from enoxaparin shows the technique may be applicable to heterogeneous samples. We are aware that many technologies have been developed for detection of the OSCS contaminant in the past decade since the heparin contamination crisis.[48−57] The most sensitive one is probably the nanometal surface energy transfer (NSET) based gold-heparin-dye nanosensor, which detected OSCS as low as 1×10^{-9}% (w/w).[52] NSET is a fluorescent detection method that relies on measuring fluorescent dyes released from the hydrolysis of their heparin conjugates attached to gold nanoparticles by heparitinase. Since enzymatic activity is inhibited by the presence of OSCS in solution, it cannot effectively detect the contamination at the higher weight percentage, such as above 10^{-3}%. On the other hand, our current data indicate that the nanopore/SVM method may only detect ∼1% contamination. By combining the nanopore/SVM with the enzymatic hydrolysis of the heparin method, we believe that it should be able to identify the contamination at a significantly lower level.

Unlike protein nanopores, the solid-state nanopores are mostly fabricated using currently available nanotechnologies, such as TEM. Thus, it is difficult to create two identical nanopores, which is one of the sources for the data variations. To address this issue, we included a standard sample as a reference in each nanopore measurement (0.1 μM HP_{dp20} in this study), to which the data from the nanopore was normalized. With this approach, we created a standard curve for the quantitation of HP_{dp20} using multiple nanopores. Our preliminary results show that the HP_{dp20} concentrations were quantified with reasonable accuracy using two nanopores. We estimate the nanopore measurement has a nM limit of detection and 5 orders of magnitude dynamic range. It is known that the heparin level in the human blood is about 1−2.4 mg/L,[58] equivalent to a range of 67−160 nM (assuming an average molecular weight of 15,000 for UFH). This implies that a nanopore device can potentially be used to monitor GAG concentrations in blood when it is integrated with a microfluidic device for sample preparation. Currently, we are working on the development of a manufacturing method to integrate an electron nanogap with the solid-state nanopore to achieve the goal of sequencing GAGs.

METHODS

Chemicals. UFH was purchased from Toronto Research Chemicals Inc. HP_{dp20} and CS_{dp20} were purchased from Iduron (product numbers H020 and CS020). Samples of enoxaparin were a gift from Dr. Christian Heiss of the Complex Carbohydrate Research Center at the University of Georgia.

Fabrication of Nanopores. Silicon chips (5×5 mm^2) coated with silicon nitride (30 nm thick) were purchased from Norcada Inc. (part number: NX5025X). Following a process of argon plasma cleaning, nanopores were drilled using the electron beam in JEOL 2010FEG and ARM 200F transmission electron microscope (TEM) at 200 keV. The size of the pores was controlled by the electron beam size and exposure time. The nanopores were imaged right after the drilling.

Preparation of Sample Solutions. Stock solutions of HP_{dp20} and CS_{dp20} were prepared respectively by dissolving the sample into H_2O. The molarity of HP_{dp20} and CS_{dp20} was determined on the basis of the assumption that heparin contains mostly trisulfated disaccharides and CS contains mostly monosulfated disaccharides. Therefore, the average molecular weight of HP_{dp20} is 6 kDa, and that of CS_{dp20} is 4.6 kDa. Their actual concentrations were determined on the basis of the carbazole assays.[59] These two stock solutions of HP_{dp20} (10 mM) and CS_{dp20} (10 mM) were used to prepare mixtures of HP_{dp20} and CS_{dp20} with a ratio of 1, 5, 10, 20, and 50% of CS_{dp20}. The final concentrations of these mixtures were diluted to be 0.5−1 μM with an electrolyte solution of 0.4 M KCl in 1 mM phosphate buffer (pH 7.4).

For the dilution study, the 10 mM stock solution of HP_{dp20} was diluted to various concentrations from a range of 1 mM to 10 nM and injected into the *cis* reservoir to make the final concentrations of the analyte 100 μM to 1 nM for the measurement.

Nanopore Measurements. A nanopore chip was first cleaned by immersing in a hot piranha solution (H_2O_2:H_2SO_4 = 1:3) for 20 min and then rinsed with Milli-Q water (a resistivity of ∼18.2 MΩ × cm

DOI: 10.1021/acsnano.9b00618
ACS Nano 2019, 13, 6308−6318

and a total organic carbon of less than 5 ppb). ***Piranha solutions are extremely energetic and may result in explosion or skin burns if not handled with extremecaution.*** After drying with N_2 gas, the nanopore chip was placed in a piranha-cleaned PCTFE cell to form a *cis* reservoir and sealed with a quick-curing silicone elastomer gasket. The PCTFE cell with a nanopore chip was then assembled with a PTFE base to form a *trans* reservoir. The electrolyte solution used was 0.4 M KCl in 1 mM phosphate buffer (pH 7.4), filtered with a Millipore 0.2 μm filter. Ag/AgCl electrodes, freshly made from Ag wires with bleach, were inserted into both *cis* and *trans* reservoirs for ionic current measurement. All of the analytes were dissolved in the electrolyte solution for the nanopore analysis.

For the measurement, both the *cis* and *trans* reservoirs were filled with the electrolyte solution, in which the nanopore was immersed for 1−2 h, followed by applying a high voltage (~1 V) between two reservoirs for 5−10 min to obtain a steady baseline current and no electrical spikes, an indicator for an open and wet nanopore. Then, an analyte solution (~10 μL) was injected into the *cis* reservoir with a final concentration of ~1 μM. A translocation bias was applied to the Ag/AgCl electrode in the *trans* reservoir, while the electrode in the *cis* reservoir was kept grounded to avoid adsorption of analyte molecules to the reference electrode. After recording the ionic current, the *cis* reservoir was drained and rinsed with the electrolyte solution by carefully removing the old buffer and replacing with a fresh buffer using a micropipette. Another baseline was recorded to ensure no contaminations were left in the *cis* reservoir before a fresh analyte solution was injected. Each SVM training session utilized 50% of experimental data (each data set contained between 500 and 2500 translocation events), and several SVM training sessions with different sets of randomly selected data were run for each comparison.

Data Collection. Ionic currents were collected at a 500 kHz sampling rate with a 100 kHz low pass filter using patch clamp amplifier Axon Axopatch 200B, with digitizer DigiData 1550A from Axon Instruments Inc. PClamp 10.4 software and an in-house developed LabView program were used for data recording. Raw data files are available upon request.

SVM Data Analysis. An in-house program written in MATLAB was used for the data process. First, a baseline of recorded ionic currents was determined by the most probable electrical current, the width of which was determined by 6σ (standard deviation) of the trace. Those spikes larger than the baseline width were recognized as translocation events. Then, each of them was subjected to Fourier transformation by down-sampling it to 20 equal frequency bins, corresponding to 25 kHz bin size. The Fourier transformed frequency spectrum was further transformed to the cepstrum domain and down-sampled into 51 equal bins (Figure S4, Supporting Information). As a result, a total of 88 signal features were created from the three domains (Table S2). To avoid features with a large numeric range from dominating those with a small numeric range, all of the calculated features were normalized to make the mean of each feature with its standard deviation between 0 and 1. We calculated the normalized correlation between different pairs of all of the features and selected one of them as a representative feature for the following analysis. The features were ranked according to the ratio between the in-group fluctuation (variation over repeated experiments of the same analyte) and the out-group fluctuation (variation between different analytes), and then, the low ranked features were removed. Those survived features were evaluated by the classification accuracy, from which an optimized set of features was chosen to achieve a maximum true positive accuracy. The SVM was run with the kernel-mode adapted from https://github.com/vjethava/svm-theta, and its running parameters C and gamma were optimized through cross-validation of a randomly selected subdata set.

Statistical Analysis. The statistical analysis was carried out in OriginPro 2017, in which the Levenberg−Marquardt algorithm was used for the curve fitting.

Computational Modeling. DFT calculations were performed using Spartan'16 for Windows, a commercially available software from Wave Function, Inc. Two-dimensional molecular structures were drawn in ChemDraw Ultra 12.0 and imported to Spartan'16 to generate corresponding 3D structures. Each structure was subjected to energy minimization using the built-in MMFF molecular mechanics prior to optimization calculation. The DFT calculations were performed at their ground-state equilibrium geometry using the B3LYP/6-31G* basis set in a vacuum.

ASSOCIATED CONTENT

Supporting Information

The Supporting Information is available free of charge on the ACS Publications website at DOI: 10.1021/acsnano.9b00618.

Additional information on GAG and nanopore characterization, analysis of translocation data, parameters used in SVM, and ways to access source data files (PDF)

AUTHOR INFORMATION

Corresponding Authors

*E-mail: Peiming.Zhang@asu.edu.
*E-mail: Stuart.Lindsay@asu.edu
*E-mail: XuWang@asu.edu

ORCID

Stuart Lindsay: 0000-0002-9364-6542
Xu Wang: 0000-0002-7369-677X
Peiming Zhang: 0000-0003-2831-2308

Notes

The authors declare the following competing financial interest(s): J.I., S.L., X.W., and P.Z. are named as inventors in a provisional patent.

ACKNOWLEDGMENTS

We would like to thank Dr. H. Deng for carrying out the carbazole assays on GAG stock solutions. This research was supported by funds from the Glycoscience Program of the NIH Common Fund (GM118339 and CA221235).

REFERENCES

(1) Bishop, J. R.; Schuksz, M.; Esko, J. D. Heparan Sulphate Proteoglycans Fine-Tune Mammalian Physiology. *Nature* **2007**, *446*, 1030−1037.

(2) Sasisekharan, R.; Shriver, Z.; Venkataraman, G.; Narayanasami, U. Roles of Heparan-Sulphate Glycosaminoglycans in Cancer. *Nat. Rev. Cancer* **2002**, *2*, 521−528.

(3) Afratis, N.; Gialeli, C.; Nikitovic, D.; Tsegenidis, T.; Karousou, E.; Theocharis, A. D.; Pavao, M. S.; Tzanakakis, G. N.; Karamanos, N. K. Glycosaminoglycans: Key Players in Cancer Cell Biology and Treatment. *FEBS J.* **2012**, *279*, 1177−1197.

(4) Mizumoto, S.; Sugahara, K. Glycosaminoglycans Are Functional Ligands for Receptor for Advanced Glycation End-Products in Tumors. *FEBS J.* **2013**, *280*, 2462−2470.

(5) Hasegawa, M.; Crowthe, R. A.; Jakes, R.; Goedert, M. Alzheimer-Like Changes in Microtubule-Associated Protein Tau Induced by Sulfated Glycosaminoglycans. *J. Biol. Chem.* **1997**, *272*, 33118−33124.

(6) Ellett, L. J.; Coleman, B. M.; Shambrook, M. C.; Johanssen, V. A.; Collins, S. J.; Masters, C. L.; Hill, A. F.; Lawson, V. A. Glycosaminoglycan Sulfation Determines the Biochemical Properties of Prion Protein Aggregates. *Glycobiology* **2015**, *25*, 745−755.

(7) Nishitsuji, K.; Uchimura, K. Sulfated Glycosaminoglycans in Protein Aggregation Diseases. *Glycoconjugate J.* **2017**, *34*, 453−466.

(8) Olczyk, P.; Mencner, L.; Komosinska-Vassev, K. Diverse Roles of Heparan Sulfate and Heparin in Wound Repair. *BioMed Res. Int.* **2015**, *2015*, 549417.

(9) Kareva, I.; Abou-Slaybi, A.; Dodd, O.; Dashevsky, O.; Klement, G. L. Normal Wound Healing and Tumor Angiogenesis as a Game of Competitive Inhibition. *PLoS One* **2016**, *11*, No. e0166655.

DOI: 10.1021/acsnano.9b00618
ACS Nano 2019, 13, 6308−6318

(10) Schnabelrauch, M.; Scharnweber, D.; Schiller, J. Sulfated Glycosaminoglycans as Promising Artificial Extracellular Matrix Components to Improve the Regeneration of Tissues. *Curr. Med. Chem.* **2013**, *20*, 2501−2523.
(11) Ly, M.; Leach, F. E., 3rd; Laremore, T. N.; Toida, T.; Amster, I. J.; Linhardt, R. J. The Proteoglycan Bikunin Has a Defined Sequence. *Nat. Chem. Biol.* **2011**, *7*, 827−833.
(12) Merry, C. L.; Lyon, M.; Deakin, J. A.; Hopwood, J. J.; Gallagher, J. T. Highly Sensitive Sequencing of the Sulfated Domains of Heparan Sulfate. *J. Biol. Chem.* **1999**, *274*, 18455−18462.
(13) Turnbull, J. E.; Hopwood, J. J.; Gallagher, J. T. A Strategy for Rapid Sequencing of Heparan Sulfate and Heparin Saccharides. *Proc. Natl. Acad. Sci. U. S. A.* **1999**, *96*, 2698−2703.
(14) Venkataraman, G.; Shriver, Z.; Raman, R.; Sasisekharan, R. Sequencing Complex Polysaccharides. *Science* **1999**, *286*, 537−542.
(15) Zaia, J. On-Line Separations Combined with MS for Analysis of Glycosaminoglycans. *Mass Spectrom. Rev.* **2009**, *28*, 254−272.
(16) Staples, G. O.; Bowman, M. J.; Costello, C. E.; Hitchcock, A. M.; Lau, J. M.; Leymarie, N.; Miller, C.; Naimy, H.; Shi, X.; Zaia, J. A Chip-Based Amide-HILIC LC/MS Platform for Glycosaminoglycan Glycomics Profiling. *Proteomics* **2009**, *9*, 686−695.
(17) Dantuluri, M.; Desai, U. R. Capillary Electrophoresis of Sulfated Molecules. *Recent Res. Devel. Anal. Biochem.* **2003**, *3*, 169−186.
(18) Lin, L.; Liu, X.; Zhang, F.; Chi, L.; Amster, I. J.; Leach, F. E., III; Xia, Q.; Linhardt, R. J. Analysis of Heparin Oligosaccharides by Capillary Electrophoresis-Negative-Ion Electrospray Ionization Mass Spectrometry. *Anal. Bioanal. Chem.* **2017**, *409*, 411−420.
(19) Sun, X.; Lin, L.; Liu, X.; Zhang, F.; Chi, L.; Xia, Q.; Linhardt, R. J. Capillary Electrophoresis-Mass Spectrometry for the Analysis of Heparin Oligosaccharides and Low Molecular Weight Heparin. *Anal. Chem.* **2016**, *88*, 1937−1943.
(20) Dekker, C. Solid-State Nanopores. *Nat. Nanotechnol.* **2007**, *2*, 209−215.
(21) Feng, Y.; Zhang, Y.; Ying, C.; Wang, D.; Du, C. Nanopore-Based Fourth-Generation DNA Sequencing Technology. *Genomics, Proteomics Bioinf.* **2015**, *13*, 4−16.
(22) Shasha, C.; Henley, R. Y.; Stoloff, D. H.; Rynearson, K. D.; Hermann, T.; Wanunu, M. Nanopore-Based Conformational Analysis of a Viral RNA Drug Target. *ACS Nano* **2014**, *8*, 6425−6430.
(23) Garalde, D. R.; Snell, E. A.; Jachimowicz, D.; Heron, A. J.; Bruce, M.; Lloyd, J.; Warland, A.; Pantic, N.; Admassu, T.; Ciccone, J.; Serra, S.; Keenan, J.; Martin, S.; McNeill, L.; Wallace, J.; Jayasinghe, L.; Wright, C.; Blasco, J.; Sipos, B.; Young, S.; Juul, S.; Clarke, J.; Turner, D. J. Highly Parallel Direct RNA Sequencing on an Array of Nanopores. *Nat. Methods* **2018**, *15*, 201−206.
(24) Zahid, O. K.; Wang, F.; Ruzicka, J. A.; Taylor, E. W.; Hall, A. R. Sequence-Specific Recognition of MicroRNAs and Other Short Nucleic Acids with Solid-State Nanopores. *Nano Lett.* **2016**, *16*, 2033−2039.
(25) Dong, Z.; Kennedy, E.; Hokmabadi, M.; Timp, G. Discriminating Residue Substitutions in a Single Protein Molecule Using a Sub-Nanopore. *ACS Nano* **2017**, *11*, 5440−5452.
(26) Waduge, P.; Hu, R.; Bandarkar, P.; Yamazaki, H.; Cressiot, B.; Zhao, Q.; Whitford, P. C.; Wanunu, M. Nanopore-Based Measurements of Protein Size, Fluctuations, and Conformational Changes. *ACS Nano* **2017**, *11*, 5706−5716.
(27) Fennouri, A.; Przybylski, C.; Pastoriza-Gallego, M.; Bacri, L.; Auvray, L.; Daniel, R. Single Molecule Detection of Glycosaminoglycan Hyaluronic Acid Oligosaccharides and Depolymerization Enzyme Activity Using a Protein Nanopore. *ACS Nano* **2012**, *6*, 9672−9678.
(28) Rivas, F.; Zahid, O. K.; Reesink, H. L.; Peal, B. T.; Nixon, A. J.; DeAngelis, P. L.; Skardal, A.; Rahbar, E.; Hall, A. R. Label-Free Analysis of Physiological Hyaluronan Size Distribution with a Solid-State Nanopore Sensor. *Nat. Commun.* **2018**, *9*, 1037.
(29) Karawdeniya, B. I.; Bandara, Y.; Nichols, J. W.; Chevalier, R. B.; Dwyer, J. R. Surveying Silicon Nitride Nanopores for Glycomics and Heparin Quality Assurance. *Nat. Commun.* **2018**, *9*, 3278.
(30) Im, J.; Biswas, S.; Liu, H.; Zhao, Y.; Sen, S.; Biswas, S.; Ashcroft, B.; Borges, C.; Wang, X.; Lindsay, S.; Zhang, P. Electronic Single-Molecule Identification of Carbohydrate Isomers by Recognition Tunnelling. *Nat. Commun.* **2016**, *7*, 13868.
(31) Onishi, A.; Ange, K. S.; Dordick, J. S.; Linhardt, R. J. Heparin and Anticoagulation. *Front. Biosci., Landmark Ed.* **2016**, *21*, 1372−1392.
(32) Chaudhari, K.; Hamad, B.; Syed, B. A. Antithrombotic Drugs Market. *Nat. Rev. Drug Discovery* **2014**, *13*, 571−572.
(33) Cajfinger, F.; Debourdeau, P.; Lamblin, A.; Benatar, V.; Falvo, N.; Benhamou, Y.; Sevestre, M. A.; Farge-Bancel, D. TROPIQUE investigators, Low-Molecular-Weight Heparins for Cancer-Associated Thrombosis: Adherence to Clinical Practice Guidelines and Patient Perception in TROPIQUE, a 409-Patient Prospective Observational Study. *Thromb. Res.* **2016**, *144*, 85−92.
(34) Piran, S.; Schulman, S. Management of Recurrent Venous Thromboembolism in Patients with Cancer: A Review. *Thromb. Res.* **2018**, *164* (Suppl 1), S172−S177.
(35) Rabenstein, D. L. Heparin and Heparan Sulfate: Structure and Function. *Nat. Prod. Rep.* **2002**, *19*, 312−331.
(36) Sasisekharan, R.; Venkataraman, G. Heparin and Heparan Sulfate: Biosynthesis, Structure and Function. *Curr. Opin. Chem. Biol.* **2000**, *4*, 626−631.
(37) Termblay, J.-F. Making Heparin Safe. *Chem. Eng. News* **2016**, *94*, 30−34.
(38) Lamari, F. N.; Karamanos, N. K., Structure of Chondroitin Sulfate. In *Chondroitin Sulfate: Structure, Role and Pharmacological Activity*; August, J. T., Granner, D., Murad, F., Eds.; Elsevier Inc.: 2006; Vol. *53*, pp 33−48.
(39) Winters-Hilt, S.; Akeson, M. Nanopore Cheminformatics. *DNA Cell Biol.* **2004**, *23*, 675−683.
(40) Kim, M. J.; McNally, B.; Murata, K.; Meller, A. Characteristics of Solid-State Nanometre Pores Fabricated Using a Transmission Electron Microscope. *Nanotechnology* **2007**, *18*, 205302/1−205302/5.
(41) Bergstrom, L.; Bostedt, E. Surface Chemistry of Silicon Nitride Powders: Electrokinetic Behaviour and ESCA Studies. *Colloids Surf.* **1990**, *49*, 183−197.
(42) Lan, W. J.; Edwards, M. A.; Luo, L.; Perera, R. T.; Wu, X.; Martin, C. R.; White, H. S. Voltage-Rectified Current and Fluid Flow in Conical Nanopores. *Acc. Chem. Res.* **2016**, *49*, 2605−2613.
(43) Keire, D. A.; Trehy, M. L.; Reepmeyer, J. C.; Kolinski, R. E.; Ye, W.; Dunn, J.; Westenberger, B. J.; Buhse, L. F. Analysis of Crude Heparin by ^{1}H NMR, Capillary Electrophoresis, and Strong-Anion-Exchange-HPLC for Contamination by Over Sulfated Chondroitin Sulfate. *J. Pharm. Biomed. Anal.* **2010**, *51*, 921−926.
(44) Lee, S.; Raw, A.; Yu, L.; Lionberger, R.; Ya, N.; Verthelyi, D.; Rosenberg, A.; Kozlowski, S.; Webber, K.; Woodcock, J. Scientific Considerations in the Review and Approval of Generic Enoxaparin in the United States. *Nat. Biotechnol.* **2013**, *31*, 220−226.
(45) Albrecht, T.; Slabaugh, G.; Alonso, E.; Al-Arif, S. M. M. R. Deep Learning for Single-Molecule Science. *Nanotechnology* **2017**, *28*, 423001/1−423001/11.
(46) Wanunu, M.; Dadosh, T.; Ray, V.; Jin, J.; McReynolds, L.; Drndic, M. Rapid Electronic Detection of Probe-Specific MicroRNAs Using Thin Nanopore Sensors. *Nat. Nanotechnol.* **2010**, *5*, 807−814.
(47) Wanunu, M.; Morrison, W.; Rabin, Y.; Grosberg, A. Y.; Meller, A. Electrostatic Focusing of Unlabelled DNA into Nanoscale Pores Using a Salt Gradient. *Nat. Nanotechnol.* **2010**, *5*, 160−165.
(48) Trehy, M. L.; Reepmeyer, J. C.; Kolinski, R. E.; Westenberger, B. J.; Buhse, L. F. Analysis of Heparin Sodium by SAX/HPLC for Contaminants and Impurities. *J. Pharm. Biomed. Anal.* **2009**, *49*, 670−673.
(49) Keire, D. A.; Mans, D. J.; Ye, H.; Kolinski, R. E.; Buhse, L. F. Assay of Possible Economically Motivated Additives or Native Impurities Levels in Heparin by ^{1}H NMR, SAX-HPLC, and Anticoagulation Time Approaches. *J. Pharm. Biomed. Anal.* **2010**, *52*, 656−664.
(50) Kang, Y.; Gwon, K.; Shin, J. H.; Nam, H.; Meyerhoff, M. E.; Cha, G. S. Highly Sensitive Potentiometric Strip Test for Detecting

DOI: 10.1021/acsnano.9b00618
ACS Nano 2019, 13, 6308−6318

High Charge Density Impurities in Heparin. *Anal. Chem.* **2011**, *83*, 3957−3962.
(51) Nemes, P.; Hoover, W. J.; Keire, D. A. High-Throughput Differentiation of Heparin from Other Glycosaminoglycans by Pyrolysis Mass Spectrometry. *Anal. Chem.* **2013**, *85*, 7405−7412.
(52) Kalita, M.; Balivada, S.; Swarup, V. P.; Mencio, C.; Raman, K.; Desai, U. R.; Troyer, D.; Kuberan, B. A Nanosensor for Ultrasensitive Detection of Oversulfated Chondroitin Sulfate Contaminant in Heparin. *J. Am. Chem. Soc.* **2014**, *136*, 554−557.
(53) Wang, W.; Han, N.; Li, R.; Han, W.; Zhang, X.; Li, F. Supercharged Fluorescent Protein as a Versatile Probe for the Detection of Glycosaminoglycans *in Vitro* and *in Vivo*. *Anal. Chem.* **2015**, *87*, 9302−9307.
(54) Lee, C. Y.; Tseng, W. L. Molecular Beacon-Based Fluorescent Assay for Specific Detection of Oversulfated Chondroitin Sulfate Contaminants in Heparin without Enzyme Treatment. *Anal. Chem.* **2015**, *87*, 5031−5035.
(55) Lester, J.; Chandler, T.; Gemene, K. L. Reversible Electrochemical Sensor for Detection of High-Charge Density Polyanion Contaminants in Heparin. *Anal. Chem.* **2015**, *87*, 11537−11543.
(56) Lee, H.; In, B.; Mehta, P. K.; Kishore, M. Y. L. N.; Lee, K.-H. Dual Role of a Fluorescent Peptidyl Probe Based on Self-Assembly for the Detection of Heparin and for the Inhibition of the Heparin-Digestive Enzyme Reaction. *ACS Appl. Mater. Interfaces* **2018**, *10*, 2282−2290.
(57) Ding, Y.; Zhou, M.; Wei, H. A Supercharged Fluorescent Protein Based FRET Sensing Platform for Detection of Heparin Contamination. *Anal. Methods* **2017**, *9*, 5593−5597.
(58) Engelberg, H. Plasma Heparin Levels in Normal Man. *Circulation* **1961**, *23*, 578−581.
(59) van den Hoogen, B. M.; van Weeren, P. R.; Lopes-Cardozo, M.; van Golde, L. M. G.; Barneveld, A.; van de Lest, C. H. A. A Microtiter Plate Assay for the Determination of Uronic Acids. *Anal. Biochem.* **1998**, *257*, 107−111.

DOI: 10.1021/acsnano.9b00618
ACS Nano 2019, 13, 6308−6318